20
Some applications

We proceed to some applications of the analysis in chapter 19. Start with closed j-shells filled up to the energy F as illustrated in Fig. 20.1, and define particle and hole operators by [Fe71]

$$\begin{aligned} a_\alpha^\dagger &\equiv c_\alpha^\dagger && ;\ \alpha > F \\ b_\alpha^\dagger &= S_{-\alpha} c_{-\alpha} && ;\ \alpha < F \end{aligned} \tag{20.1}$$

Recall that the phase S_α is defined by

$$S_\alpha \equiv (-1)^{j_\alpha - m_{j_\alpha}} (-1)^{\frac{1}{2} - m_{t_\alpha}} \tag{20.2}$$

Equations (20.1) form a *canonical transformation* since they leave the anti-commutation relations in Eqs. (19.30) unchanged. Denote by $|0\rangle$ the non-interacting ground state illustrated in Fig. 20.1. Both particle and hole destruction operators annihilate this state

$$a_\alpha |0\rangle = b_\alpha |0\rangle = 0 \tag{20.3}$$

Furthermore, by Eq. (19.31) and the discussion following Eq. (19.33), both $a^\dagger$ and $b^\dagger$ are irreducible tensor operators (ITO).

To illustrate the physics and theoretical techniques, we consider some model cases. Equations (19.35) form the starting point of this analysis.

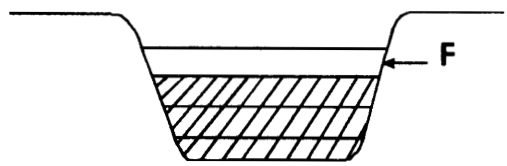

Fig. 20.1. Closed j-shells as a basis for defining particle and hole operators.

https://doi.org/10.1017/9781009290616.025 Published online by Cambridge University Press

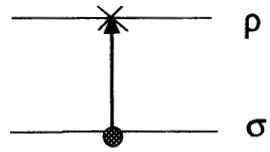

Fig. 20.2. A particle–particle transition.

Consider first a particle–particle transition from the single-particle state σ to the state ρ as illustrated in Fig. 20.2. Take

$$\begin{aligned} |\Psi_i\rangle &= a_\sigma^\dagger|0\rangle \\ |\Psi_f\rangle &= a_\rho^\dagger|0\rangle \end{aligned} \tag{20.4}$$

Here $\rho = (n_r l_r \tfrac{1}{2} j_r m_{j_\rho}; \tfrac{1}{2} m_{t_\rho}) \equiv (r; m_{j_\rho} m_{t_\rho})$ with a similar relation for σ. In this case one has the very simple result that the quantum numbers a must refer to the final state and b to the initial state

$$\psi_{J,T}^{fi}(ab) = \delta_{ar}\delta_{bs} \qquad ; \text{ particle–particle} \tag{20.5}$$

All the angular momentum and isospin algebra has now been dealt with in arriving at the doubly reduced matrix elements. Note that here and henceforth we adopt the convention that the selection rules on J and T are implicitly contained in the reduced matrix elements.

The proof of Eq. (20.5) goes as follows. The only term in the operator $\hat{\zeta}^\dagger$ which contributes to the transition in this case is

$$\hat{\zeta}^\dagger(ab; JM_J, TM_T) \doteq \delta_{ar}\delta_{bs}[a_\rho^\dagger \odot S_{-\sigma} a_{-\sigma}]_{JM_J TM_T} \tag{20.6}$$

Now take the matrix element

$$\begin{aligned} \langle\Psi_f|\hat{\zeta}^\dagger(rs; JM_J, TM_T)|\Psi_i\rangle &= S_\sigma \langle j_\rho m_{j_\rho} j_\sigma, -m_{j_\sigma}|j_\rho j_\sigma JM_J\rangle \\ &\quad \times \langle \tfrac{1}{2} m_{t_\rho} \tfrac{1}{2}, -m_{t_\sigma}|\tfrac{1}{2}\tfrac{1}{2} TM_T\rangle \end{aligned} \tag{20.7}$$

This is just one form of the Wigner–Eckart theorem [Ed74]

$$\begin{aligned} \text{l.h.s.} &= S_\sigma \langle j_\rho m_{j_\rho} j_\sigma, -m_{j_\sigma}|j_\rho j_\sigma JM_J\rangle \langle \tfrac{1}{2} m_{t_\rho} \tfrac{1}{2}, -m_{t_\sigma}|\tfrac{1}{2}\tfrac{1}{2} TM_T\rangle \\ &\quad \times \frac{1}{\sqrt{(2J+1)(2T+1)}} \langle \Psi_f \vdots\vdots \hat{\zeta}^\dagger(rs; JT) \vdots\vdots \Psi_i\rangle \end{aligned} \tag{20.8}$$

A comparison of these two equations gives the stated result.

Consider next the somewhat more complicated case of a particle–hole transition as illustrated in Fig. 20.3. Here a particle makes a transition out of the filled ground state, leaving a hole behind. In this case one has

https://doi.org/10.1017/9781009290616.025 Published online by Cambridge University Press

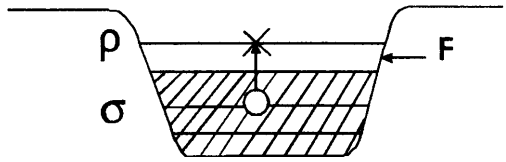

Fig. 20.3. A particle–hole transition.

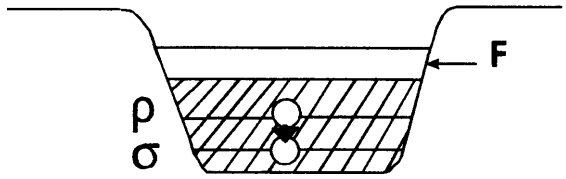

Fig. 20.4. A hole–hole transition.

$$\begin{aligned} |\Psi_i\rangle &= |0\rangle \\ |\Psi_f\rangle &= [a_\rho^\dagger \odot b_\sigma^\dagger]_{JM_J;TM_T}|0\rangle \end{aligned} \tag{20.9}$$

In this case, the only contributing term in the operator $\hat{\zeta}^\dagger$ is

$$\hat{\zeta}^\dagger(ab;JM_J,TM_T) \doteq \delta_{ar}\delta_{bs}\,[a_\rho^\dagger \odot b_\sigma^\dagger]_{JM_JTM_T} \tag{20.10}$$

Now take matrix elements and use the orthonormality of the Clebsch–Gordon (C–G) coefficients [Ed74]

$$\begin{aligned} \langle\Psi_f|\hat{\zeta}^\dagger(rs;JM_J,TM_T)|\Psi_i\rangle &= 1 \\ &= \frac{1}{\sqrt{(2J+1)(2T+1)}}\langle J,T\,\vdots\!\vdots\,\hat{\zeta}^\dagger(rs;JT)\,\vdots\!\vdots\,0\rangle \end{aligned} \tag{20.11}$$

The Wigner–Eckart theorem has again been used to obtain the second equality. Thus, in this case also, one has the simple result

$$\psi_{J,T}^{fi}(ab) = \delta_{ar}\delta_{bs} \qquad ;\ \text{particle–hole} \tag{20.12}$$

Consider the most complicated case of a hole–hole transition as illustrated in Fig. 20.4. Here the initial state has a hole in the state ρ and the final state a hole in σ. The transition is actually accomplished, of course, by a particle going in the opposite direction. In this case

$$\begin{aligned} |\Psi_i\rangle &= b_\rho^\dagger|0\rangle \\ |\Psi_f\rangle &= b_\sigma^\dagger|0\rangle \end{aligned} \tag{20.13}$$

The contributing term in $\hat{\zeta}^\dagger$ is

$$\hat{\zeta}^\dagger(ab;JM_J,TM_T) \doteq \delta_{ar}\delta_{bs}[S_\rho b_{-\rho} \odot b_\sigma^\dagger]_{JM_JTM_T} \tag{20.14}$$

https://doi.org/10.1017/9781009290616.025 Published online by Cambridge University Press

One has to first turn the destruction and creation operators around in computing the matrix element.[1] Use of the basic anti-commutation relations gives

$$\hat{\zeta}^{\dagger}(ab;JM_J,TM_T) \doteq \delta_{ar}\delta_{bs}\left\{\delta_{J0}\delta_{T0}\sqrt{2(2j_a+1)}\,\delta_{rs} -(-1)^{j_a+j_b-J}(-1)^{\frac{1}{2}+\frac{1}{2}-T}[b^{\dagger}_{\sigma}\odot S_{\rho}b_{-\rho}]_{JM_JTM_T}\right\} \quad (20.15)$$

Here the anti-commutation relations for the b's has been employed, along with the relation for reversing the order of coupling in the C–G coefficients [Ed74]

$$\langle j_\rho m_{j_\rho} j_\sigma m_{j_\sigma}|j_\rho j_\sigma JM_J\rangle = (-1)^{j_\rho+j_\sigma-J}\langle j_\sigma m_{j_\sigma} j_\rho m_{j_\rho}|j_\sigma j_\rho JM_J\rangle \quad (20.16)$$

There is a similar relation for isospin. The first term in Eq. (20.15), now simply a c-number, follows from

$$\begin{aligned}&\sum_{m_{j_\rho}}\langle j_\rho m_{j_\rho} j_\rho,-m_{j_\rho}|j_\rho j_\rho JM_J\rangle(-1)^{j_\rho-m_{j_\rho}}\\ &=\sum_{m_{j_\rho}}\langle j_\rho m_{j_\rho} j_\rho,-m_{j_\rho}|j_\rho j_\rho JM_J\rangle\langle j_\rho m_{j_\rho} j_\rho,-m_{j_\rho}|j_\rho j_\rho 0\,0\,\rangle\sqrt{2j_\rho+1}\\ &=\sqrt{2j_\rho+1}\,\delta_{J0}\end{aligned} \quad (20.17)$$

Again, there is a similar relation for isospin.

Now the calculation of the remaining matrix element proceeds exactly as in the particle–particle case. Note that here $S_{-\rho}=S_\rho$.

$$\begin{aligned}\psi^{fi}_{J,T}(ab) &= \delta_{ar}\delta_{bs}\delta_{rs}\delta_{J0}\,\delta_{T0}\,[2(2j_a+1)(2T_i+1)(2J_i+1)]^{1/2}\\ &\quad -(-1)^{j_a+j_b-J}(-1)^{\frac{1}{2}+\frac{1}{2}-T}\delta_{ar}\delta_{bs} \qquad ;\ \text{hole–hole}\end{aligned} \quad (20.18)$$

The reduced matrix element has been calculated in the first (scalar) term, and we now observe that there will, in fact, be an additional contribution $\psi^{fi}_{0,0}(aa)$ of this type of term for each occupied shell $a<F$ in Fig. 20.1.

Suppose one does elastic scattering from a ground state that has neither particles nor holes as in Fig. 20.1

$$|\Psi_i\rangle = |\Psi_f\rangle = |0\rangle \quad (20.19)$$

In this case, the only non-zero contribution comes from the first term in Eq. (20.18), and from Eq. (19.38) one has

$$\langle 0||\hat{M}_0(\kappa)||0\rangle = \sum_{a<F}\sqrt{2j_a+1}\,\langle a||M^{(0)}_0(\kappa)||a\rangle \quad (20.20)$$

[1] They must be *normal-ordered*.

https://doi.org/10.1017/9781009290616.025 Published online by Cambridge University Press

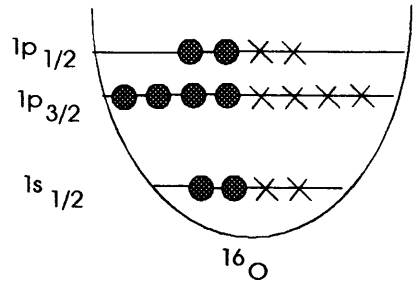

Fig. 20.5. Shell model for $^{16}_{8}$O ground state.

Now consider the case of elastic scattering from a $(J^\pi, T) = (0^+, 0)$ target. In this case, the only contributing multipole is $\hat{M}_0(\kappa)$, and one evidently measures the Fourier transform of the ground-state charge density

$$\sqrt{4\pi}\,\langle\Psi_0|\hat{M}_{00}(\kappa)|\Psi_0\rangle = \int d^3x \left[\frac{\sin\kappa x}{\kappa x}\right]\rho_{00}(\mathbf{x}) \tag{20.21}$$

As an example, consider $^{16}_{8}$O modeled as indicated in Fig. 20.5. In this case, Eq. (20.20) gives

$$\begin{aligned}\langle 0||\hat{M}_0(\kappa)||0\rangle &= \sqrt{2}\,\langle 1s_{1/2}||M_0^{(0)}(\kappa)||1s_{1/2}\rangle + \sqrt{4}\,\langle 1p_{3/2}||M_0^{(0)}(\kappa)||1p_{3/2}\rangle \\ &\quad + \sqrt{2}\,\langle 1p_{1/2}||M_0^{(0)}(\kappa)||1p_{1/2}\rangle\end{aligned} \tag{20.22}$$

Use of the tables in [Do79] then gives for harmonic oscillator wave functions

$$\sqrt{4\pi}\,\langle\Psi_0||\hat{M}_0(\kappa)||\Psi_0\rangle = 8\left(1 - \frac{1}{2}y\right)e^{-y} \tag{20.23}$$

Note that at $\kappa = 0$ one must obtain Z, the total charge on the nucleus, and this result is indeed recovered. Since s and p radial wave functions contribute here, the coefficient of e^{-y} is a first-order polynomial in y. Thus there is (at most) one diffraction zero as a function of y. Figure 20.6 shows the fit to the experimental charge form factor in this model [Do75]. The data is from [Mc69]. There is one parameter in this fit, $b_{\text{osc}} = 1.77$ fm. Also shown is the result obtain with Woods–Saxon radial wave functions, where a second diffraction minimum is observed [Do69]. Note that the harmonic oscillator wave functions provide an excellent description of the gross distribution of charge, and only break down when one seeks a more detailed description at higher momentum transfer.

Figure 4.2 shows the quality of elastic (e, e) data presently available. Figure 21.5 in the next section illustrates the quality of the nuclear charge distribution which can now be extracted from elastic (e, e) charge scattering. Note the small uncertainty band on the experimental result in that figure.

https://doi.org/10.1017/9781009290616.025 Published online by Cambridge University Press

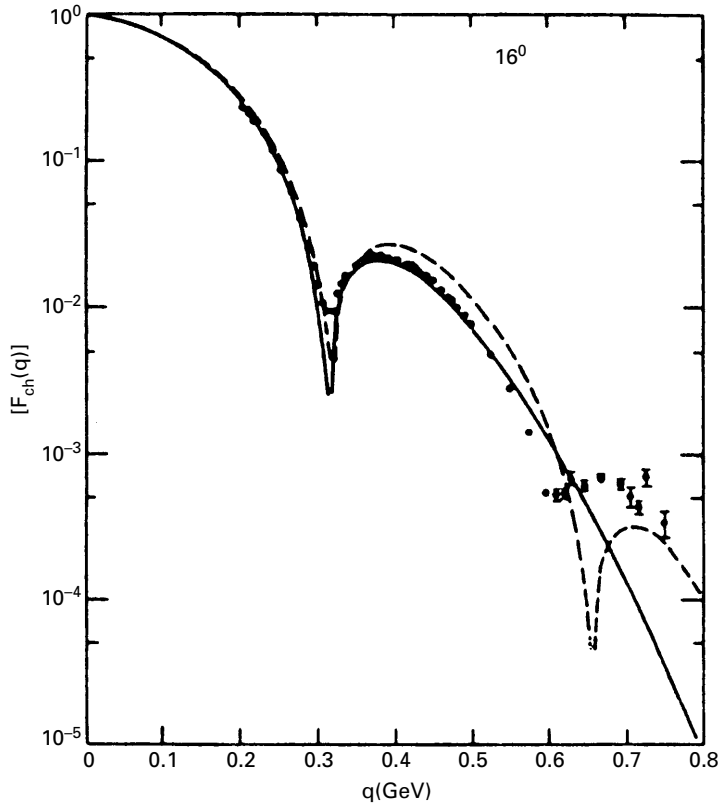

Fig. 20.6. Elastic charge form factor for $^{16}_{8}$O showing results using harmonic oscillator (solid curve) and Woods–Saxon (dashed curve) radial wave functions [Do69, Do75, Mc69].

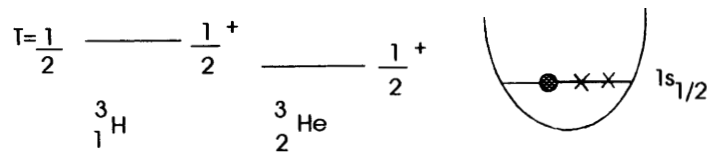

Fig. 20.7. Ground states of $^{3}_{2}$He and $^{3}_{1}$H.

Consider elastic magnetic scattering. It is proven in appendix E that only the odd magnetic multipoles contribute to elastic scattering through the transverse interaction. Consider the simplest nuclear case of elastic scattering from $^{3}_{2}$He and $^{3}_{1}$H with $(J^{\pi}, T) = (\frac{1}{2}^{+}, \frac{1}{2})$ as illustrated in Fig. 20.7. Here only $\hat{T}_1^{\text{mag}}(\kappa)$ contributes. Although very sophisticated three-body calculations are available for this system (see later), we consider it here as a very simple illustration.

https://doi.org/10.1017/9781009290616.025 Published online by Cambridge University Press

Table 20.1. Comparison of experimental and theoretical magnetic moments of the three-nucleon system calculated in the harmonic oscillator shell model.

	$\mu(^3\mathrm{H}) + \mu(^3\mathrm{He})$	$\mu(^3\mathrm{H}) - \mu(^3\mathrm{He})$
Theory	0.8795	4.7059
Experiment	0.8513	5.1064

The shell model configuration in Fig. 20.7 is a $(1s_{1/2})^{-1}$ hole in the $1s$ shell. Use of Eq. (20.18) in this case leads to

$$\psi_{JT}[(1s_{1/2})^2] = 4\delta_{J0}\delta_{T0} - (-1)^{J+T} \tag{20.24}$$

From the general result in Eq. (19.38), and the tables in [Do79], one finds

$$\begin{aligned}
\left(\frac{4\pi}{2}\right)^{1/2} \langle \frac{1}{2}^+ ; \frac{1}{2} m_t || \hat{M}_0(\kappa) || \frac{1}{2}^+ ; \frac{1}{2} m_t \rangle &= \left(\frac{3}{2} + m_t\right) e^{-y} \\
&= Z\, e^{-y} \\
i \left(\frac{4\pi}{2}\right)^{1/2} \langle \frac{1}{2}^+ ; \frac{1}{2} m_t || \hat{T}_1^{\mathrm{mag}}(\kappa) || \frac{1}{2}^+ ; \frac{1}{2} m_t \rangle & \\
&= -\sqrt{2} \left(\frac{\kappa}{2m}\right) \left[\frac{1}{2}(\mu_p + \mu_n) - m_t(\mu_p - \mu_n)\right] e^{-y} \\
&= -\sqrt{2} \left(\frac{\kappa}{2m}\right) \mu\, e^{-y}
\end{aligned} \tag{20.25}$$

Here Z is the charge of the target and μ its magnetic moment. The proportionality of the matrix element of $\hat{T}_1^{\mathrm{mag}}$ to the magnetic moment is a general result as shown in appendix A. At higher κ one probes the spatial distribution of the magnetic moment distribution. Table 20.1 shows the (well-known) comparison between the calculated and experimental magnetic moments for this system.

Figure 20.8 shows the low-κ elastic (e, e) data compared with this shell model calculation with an oscillator parameter chosen as $b_{\mathrm{osc}} = 1.59$ fm [Do76, Wa95]. Again, it is only the *deviations* from these simple results that show up the more sophisticated elements of nuclear structure, to which we shall return.

With higher nuclear angular momentum J_i, higher multipoles can contribute to elastic scattering. It is shown in appendix E that parity and time-reversal invariance of the strong and electromagnetic interactions imply that only the even charge multipoles and odd transverse magnetic multipoles can contribute in the elastic case. Consider a $1g_{9/2}$ proton as the single-particle shell model assignment for the ground state of $^{93}_{41}\mathrm{Nb}$ as depicted in Fig. 20.9. The *highest* magnetic multipole that can contribute in this case is $\hat{T}_9^{\mathrm{mag}}(\kappa)$. Use of the previous particle–particle results and

https://doi.org/10.1017/9781009290616.025 Published online by Cambridge University Press

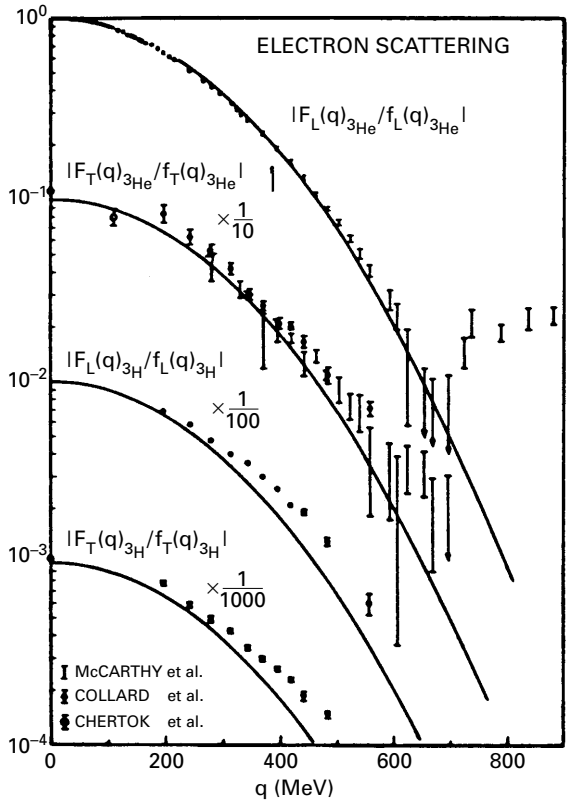

Fig. 20.8. Longitudinal and transverse elastic scattering form factors for the three-nucleon system compared with harmonic oscillator shell model results. Here $f_L = Zf_{SN}/\sqrt{4\pi}$ and $f_T = (\kappa/2m)\mu f_{SN}/\sqrt{2\pi}$. The correction factor f_{CM} has been included. [Do76, Wa84]. Data from [Co65, Ch69, Mc70].

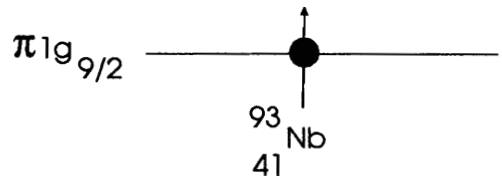

Fig. 20.9. Single-particle shell model assignment for the ground state of $^{93}_{41}$Nb.

the tables in [Do79] gives

$$\langle \frac{9}{2}^+ \,||\hat{T}_9^{\mathrm{mag}}(\kappa)||\, \frac{9}{2}^+ \rangle = \langle \pi 1g_{9/2}||T_9(\kappa)||\pi 1g_{9/2}\rangle = -\frac{2^5}{3^2\sqrt{5\cdot 11\cdot 13\cdot 17}}\, y^4 e^{-y} \left(\frac{\kappa\mu_p}{2m}\right) \tag{20.26}$$

https://doi.org/10.1017/9781009290616.025 Published online by Cambridge University Press

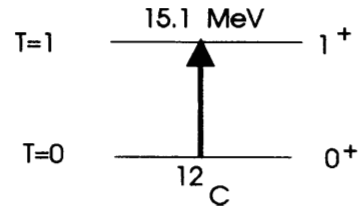

Fig. 20.10. M1 transition in $^{12}_{6}$C as example of particle–hole transition.

Note that only the intrinsic magnetization contributes to the highest multipole in the stretched configuration $j = l + \frac{1}{2}$, and note the simplicity of this result. Note also that this multipole has the highest possible number of powers of y, which implies that it will be the dominant contribution at high momentum transfer κ. The experimental results for elastic magnetic scattering from $^{93}_{41}$Nb have already been shown in Fig. 12.4.[2] In contrast to the case with real photon interactions where the long-wavelength limit is relevant and the *lowest* multipole dominates (appendix A), here the rank of the dominant multipole increases as the momentum transfer is increased until at high κ the dominant contribution is indeed M9 — one can effectively *dial* the multipole one wants to examine.

What does one learn from this? Figure 12.5 shows the surface of half-maximum intrinsic magnetization density $\mu(x)_{\max}/2$ for $^{51}_{23}$V (chosen so that it would fit on a 10 fm square). Here the configuration assignment is $(1f_{7/2})_\pi$, and the nucleus is aligned so that its angular momentum points along the z-axis with $m_j = j$. The intrinsic magnetization maps the location of the valence nucleon. The nucleus is a small magnet with a current loop provided by the motion of the orbiting proton. Elastic magnetic electron scattering at all κ provides a microscope to see the spatial structure of this small current loop [Do73].

As an example of particle–hole states consider the celebrated isovector M1 transition to the $(1^+, 1)$ state at 15.11 MeV in $^{12}_{6}$C as illustrated in Fig. 20.10. Make the simplest shell model assignments

$$\begin{aligned} |\Psi_i\rangle &= |0\rangle \\ |\Psi_f\rangle &= [a^\dagger_{1p_{1/2}} \odot b^\dagger_{1p_{3/2}}]_{1^+,1}\,|0\rangle \end{aligned} \tag{20.27}$$

Then from the above discussion of particle–hole transitions and the tables

[2] Here $q_{\text{eff}} \equiv \kappa$.

https://doi.org/10.1017/9781009290616.025 Published online by Cambridge University Press

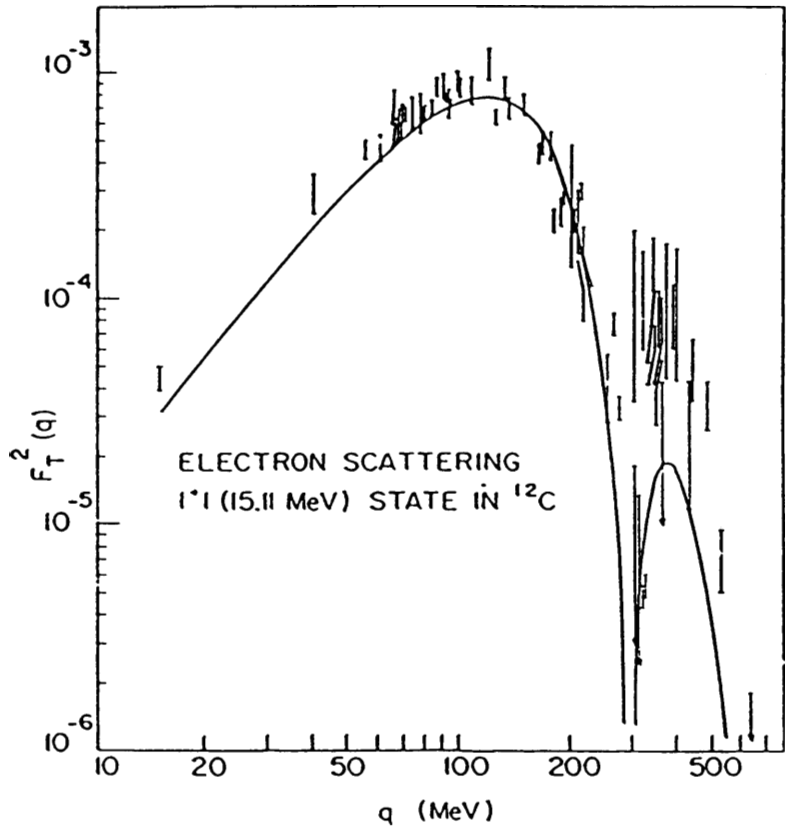

Fig. 20.11. The quantity $F_T^2(\kappa)$ for the $1^+, 1$ state in $^{12}_{6}$C(15.11 MeV). The curve is a best fit with $b_{\rm osc} = 1.77$ fm and $\xi = 2.25$ [Do75]. Here $q \equiv \kappa$.

in [Do79] one finds

$$i\sqrt{4\pi}\,\langle 1^+, 1\,0||\hat{T}_1^{\rm mag}(\kappa)||0^+, 0\rangle = i\left(\frac{4\pi}{2}\right)^{1/2}\langle 1p\frac{3}{2}||T_1^{\rm mag\,(1)}(\kappa)||1p\frac{3}{2}\rangle$$
$$= \frac{2}{3}\left(\frac{\kappa}{2m}\right)\left[1 - 2(\mu_p - \mu_n)\left(1 - \frac{1}{2}\,y\right)\right]e^{-y} \tag{20.28}$$

Now it is clear that the model of a pure particle–hole transition is an oversimplification. With configuration mixing, even within just the $1p$-shell, the amplitudes in Eq. (19.28) will be changed from the pure particle–hole value, and in general reduced from this value. A fit to the experimental data for this transition using Eq. (20.28) with an oscillator parameter $b_{\rm osc} = 1.77$ fm and an overall reduction factor of $\xi = 2.25$ is shown in Fig. 20.11 [Do75].[3]

[3] In this figure $d\sigma/d\Omega \equiv 4\pi\sigma_M[(q^4/\mathbf{q}^4)F_L^2 + (q^2/2\mathbf{q}^2 + \tan^2\theta/2)F_T^2]r$.

https://doi.org/10.1017/9781009290616.025 Published online by Cambridge University Press

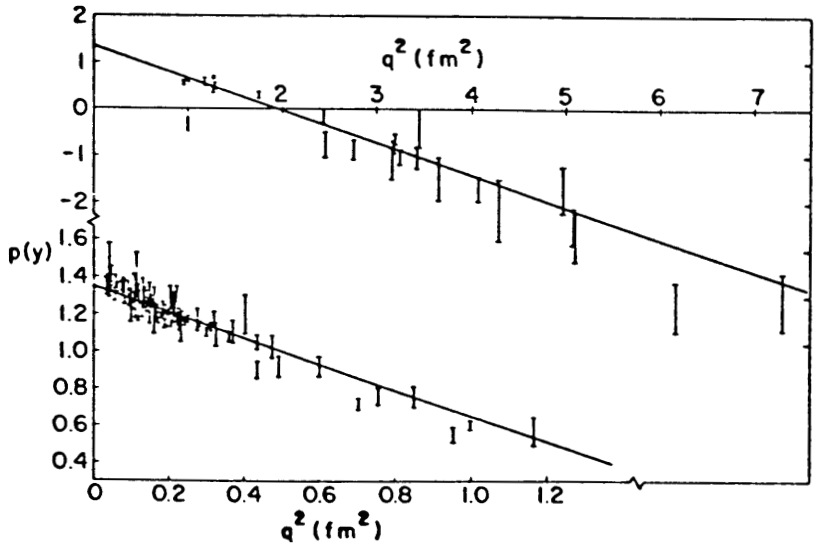

Fig. 20.12. Inelastic electron scattering to the $1^+, 1$ state in $^{12}_{6}$C(15.11 MeV) plotted in terms of the polynomial $p(y)$ in Eq. (20.29). The straight line is a fit with $1p$-shell harmonic oscillator wave functions [Do79a]. Again, $q \equiv \kappa$.

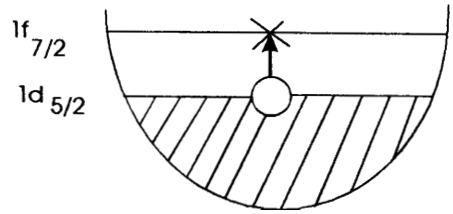

Fig. 20.13. Particle–hole configuration $(1f_{7/2})(1d_{5/2})^{-1}$.

If both the ground and excited states are configuration mixed, but still both described within the $1p$-shell oscillator model, then the polynomial in the above transition amplitude must indeed be of the form

$$p(y) = \alpha_0 - \alpha_1 y \tag{20.29}$$

Figure 20.12 shows such a straight-line fit to the data [Do79a]. This fit determines two of the four possible one-body amplitudes $\psi^{fi}_{J,T}(ab)$ for this transition, if it is indeed described within the $1p$-shell oscillator model. Note that this straight-line plot, now on a *linear* scale, gives some credence to this description.

As an example of magnetic excitation of high-spin states, consider the isovector transition to the stretched member $(6^-, 1)$ of the particle–hole

https://doi.org/10.1017/9781009290616.025 Published online by Cambridge University Press

configuration in Fig. 20.13. Model the ground and excited states by

$$\begin{aligned} |\Psi_i\rangle &= |0\rangle \\ |\Psi_f\rangle &= [a^\dagger_{1f_{7/2}} \odot b^\dagger_{1d_{5/2}}]_{6^-,1}\,|0\rangle \end{aligned} \tag{20.30}$$

Then, as before,

$$\begin{aligned} i\sqrt{4\pi}\,\langle 6^-, 1\,0||\hat{T}^{\rm mag}_6(\kappa)||0^+,0\rangle &= i\left(\frac{4\pi}{2}\right)^{1/2}\langle 1f\frac{7}{2}||T^{{\rm mag}\,(1)}_6(\kappa)||1d\frac{5}{2}\rangle \\ &= -\left(\frac{\kappa}{2m}\right)(\mu_p-\mu_n)\frac{2^3}{3\sqrt{3\cdot 11}}\,y^{5/2}\,e^{-y} \end{aligned} \tag{20.31}$$

Note the simplicity of this result. Again, only the magnetization contributes to this highest multipole in the stretched configuration, and this multipole gives the maximum power of y. The large isovector magnetic moment of the nucleon in Eq. (19.4) implies that isovector transitions are preferentially excited in electron scattering at large scattering angles and high momentum transfers. Figure 12.6 shows a spectrum for $^{24}_{12}$Mg taken under these conditions, and the transverse form-factor squared for the state at 15.0 MeV which dominates the spectrum; it is evidently a 6^-.[4] Such stretched particle–hole states have now been seen throughout the periodic table, including states as high as 14^- in $^{208}_{82}$Pb [Li79].

[4] Note that even though $^{24}_{12}$Mg is not the closed $1d_{5/2}$-shell nucleus of the shell model (that would be $^{28}_{14}$Si), the $(6^-,1)$ particle–hole transition still shows up strongly in the spectrum.

https://doi.org/10.1017/9781009290616.025 Published online by Cambridge University Press